

An Examination of the Spring 1997 Mid-latitude East Pacific

Sea Surface Temperature Anomaly

Randy G. Brown and Lee-Lueng Fu

MS 300-323  
Jet Propulsion Laboratory  
California Institute of Technology  
4800 Oak Grove Drive  
Pasadena, CA 91109

July, 1999

### Abstract

We seek to document and explain the lifecycle of the warm SST anomaly that intensified and weakened off the west coast of the United States to peak anomalies of  $4^{\circ}$  K during April-June 1997. We use remotely sensed observational data and model analyses to compute an energy budget for the warm anomaly. The bulk of the anomalous warming was confined to the top 50m of ocean and occurred during May. The immediate cause for the warming was twofold: latent heat fluxes decreased in magnitude as a result of both lower wind speeds and positive moisture anomalies, while the net radiative flux into the ocean increased as a result of lower than normal fractional cloud coverage. During June, the wind speed strengthened and became northerly, resulting in larger than normal latent and sensible heat fluxes that weakened the SST anomaly. Examination of NCEP 1000 mb geopotential height for May shows that the Aleutian low extended far south of its usual position and was responsible for the weaker southerly winds and suppressed latent heat fluxes in the warm anomaly area. Finally, we note that the near simultaneous appearance of this warm anomaly in conjunction with warm El Niño waters off Peru makes El Niño an unlikely trigger for the northeast Pacific warm anomaly. We suggest a possible alternate scenario in which both events are remotely triggered by the 30-60 day intraseasonal oscillation.

## 1 Introduction

During April of 1997, a  $\sim 1^\circ \text{ K}$ ,  $10^6 \text{ km}^2$  warm sea surface temperature (SST) anomaly that had lingered for nearly a year off the west coast of California began to rapidly intensify. The warm anomaly expanded in area and reached a peak intensity of  $4^\circ \text{ K}$  in May, and then rapidly weakened in June. The anomalously warm ocean waters drew warm-water fish such as sardines, yellowfin tuna, and bonito northward, attracting the attention of fisheries and marine biologists (San Francisco Chronicle, 1997). The intensification of the warm anomaly was accompanied by a marked decrease in cloudiness in May, and occurred at nearly the same time that warm waters first appeared off the west coast of Peru with the onset of the 1997-1998 El Niño. We undertake in this paper an examination of the underlying causes of the rapid warming and cooling of the SST anomaly during April-June of 1997, and seek to identify the specific physical mechanisms responsible for creating this event.

The variability of SST in the North Pacific has been the focus of a number of observational and modeling studies. The large scale spatial structure of nonseasonal modes of variability has been examined using Empirical Orthogonal Functions (EOF) of observed SST, resulting in the identification of a dominant mode of variability related to El Niño (Weare et al [1976], Deser and Blackmon [1995], Hsiung and Newell [1983], and others). This mode, shown in Figure 1a (reproduced from Weare et al [1976]), bears some resemblance to the distribution of the anomalous SST observed during April and May of 1997 (Figure 1b), particularly with respect to the cold anomaly in the central North Pacific and the presence of the warm El Niño waters in the eastern equatorial Pacific. However, the coastal warm anomaly in Figure 1b does not stretch along the entire coastline and extends much further west than the coastal warm anomaly in the EOF. In addition, the EOF does not show the anomalously warm waters present to the north of the cold anomaly in the central North Pacific seen in Figure 1b.

An important feature of the anomalous SST is that the same spatial structure can be seen in the average over the 15 months preceding April 1997, with the difference that the equatorial waters were anomalously cold and hence out of phase with the warming off the west coast of California (Figure 1c). The spatial structure of the warm anomaly was already in place well before the 1997-1998 El Niño, eliminating the possibility that El-Niño itself triggered the warm anomaly via an atmospheric teleconnection. The intensification of the warm anomaly during April and May occurred nearly simultaneously with the appearance of warm water off Peru, so it too was not likely a consequence of El Niño. A more plausible scenario, which we discuss in the final section, is that *both* the warm anomaly and El Niño were triggered by a third atmospheric event.

To develop an explanation for the April-June SST transient, we use a variety of observational data sets to determine, at least to zeroth order, the local SST forcings responsible for the observed change in SST. We then examine possible links between these local forcings and larger scale dynamics. The lack of surface data in the area of the warm anomaly necessitates the use of satellite data and model analyses, which we discuss in section two. The details of the warm anomaly itself and its uniqueness when compared to the previous 16 years of SST data is discussed in section 3, and the energy budget and error analyses are described in sections 4 and 5. Finally, we discuss links between the large scale dynamics, stratus clouds, and local SST forcings in section 6.

## 2 Data

Understanding the immediate cause of the SST anomaly requires computation of an energy budget for the volume of water under consideration. Such a calculation at a minimum requires SST, surface wind speed, surface pressure, ocean mixed layer temperature and velocities, cloudiness (for radiative flux calculations), and surface water vapor and air temperature data. For SST data we use the weekly one degree resolution Reynold's SST data set for 1982 through July 1997. This data set is

created from a combination of ship, buoy, and Advanced Very High Resolution Radiometer (AVHRR) satellite data using optimum interpolation analysis as described in Reynolds and Smith [1994].

Surface wind speed measurements were made during the period of the warm anomaly by the NASA Scatterometer (NSCAT) carried aboard the Japanese Space Agency Advanced Earth Observing satellite (ADEOS). Before the failure of the ADEOS satellite on 29 June 1997, NSCAT successfully measured surface wind speed with 25 km resolution, and covered 90 percent of the ice-free ocean surface every two days with 1.3 m/s accuracy (Freilich and Dunbar, 1999). For the purpose of this study, the level 2 NSCAT data was gridded on a one degree grid using a successive correction technique, and then weekly averaged using Wednesday centered weeks as used for the Reynold's SST data.

Because the NSCAT data set is of limited length, it can not be used to determine the seasonal climatology of the surface wind field for use in the energy budget calculations. For this purpose we use the ECMWF surface wind field and/or the Special Sensor Microwave Imager (SSM/I) surface wind field. The ECMWF wind field was interpolated from the original 2.5° grid to the Reynold's 1° grid, and the wind speed was computed for each day of data before creating weekly or monthly averages. Monthly averaged SSM/I wind data on 1° grid was obtained from Remote Sensing Systems, Inc. (Wentz, 1997) for the years 1987-1997; data for March-June 1987 is missing.

Depth dependent ocean temperature, salinity, and horizontal velocity data was obtained from the archived weekly National Center for Environmental Prediction (NCEP) Pacific ocean analyses. This data is available from NCEP on a 1.5 degree longitude by 1.0 degree latitude grid. The data for 1997 consists of weekly averaged data, while the data for the years 1980-1996 is monthly averaged. NCEP daily global atmospheric operational analyses are used for analysis of geopotential height at levels above the surface for 1997, while the NCEP/NCAR Reanalysis data set is used for 1979-1996 (both the NCAR/NCEP Reanalysis and Operational Analysis data are provided through the NOAA

Climate Diagnostics Center). The NCEP reanalyzed daily 2m air temperature and sea level pressure data are also used. This data is interpolated onto a  $1^\circ$  grid before being weekly or monthly averaged.

The small number of direct surface relative humidity observations and the lack of dynamical constraints on relative humidity make determination of that variable difficult on time scales of a week or less. This problem is compounded by the importance of surface air specific humidity ( $q_{air}$ ) in latent heat flux calculations. To overcome this, we compute  $q_{air}$  using the method of Liu (1986), which determines the monthly averaged  $q_{air}$  using satellite observed column water vapor (see section 4 for more details). For these calculations, we use the monthly averaged SSM/I column water vapor data, again provided by RSS, Inc. This dataset is on the same grid and has the same data gaps as the SSM/I wind data discussed previously.

Another SSM/I related dataset used in this study is the monthly averaged cloud fraction data set available from the National Climatic Data Center for the years 1987-1997, based on the work of Weng et al [1997]. The cloud fraction in this dataset is calculated as the fraction of pixels with liquid water path (as determined from 85 Ghz SSM/I data) exceeding a threshold of 0.02 mm over a one month time period in a 2.5 degree grid [Weng et al 1997].

### 3 Physical Description of Event

The warm SST anomaly that had existed off the west coast of California for over a year began to intensify during April 1997, when the SST anomaly was located in the vicinity of 35N, 138W. At this time, the SST anomaly had peak temperatures of about 2 K, and covered a roughly 8 by 8 degree ( $\sim 6 * 10^{11} \text{km}^2$ ) area (Figure 2a). Note that the plan view plots of anomalous SST shown in Figure 2 were made by subtracting the 1982-1997 SST mean for a given week from the actual SST for that week. Over the next seven weeks, the warm anomaly moved eastward and expanded in size up to a peak area of  $12^\circ \times 12^\circ$ . The intensity of the SST anomaly also grew, with peak temperature reaching

over  $4^{\circ}$  K in late May. The SST anomaly suddenly decreased in size and intensity during the week of June  $8^{th} - 14^{th}$ , and by June  $22^{nd} - 28^{th}$  covered an area of  $\sim 4^{\circ} \times 4^{\circ}$ , with a peak anomalous SST of  $\sim 2^{\circ}$  K.

Figure 2 also shows the evolution of the weekly averaged NSCAT surface wind field; note that this is not the anomalous wind, and that the barbs represent the *tails* of the wind vectors. In a normal year, one generally finds a gradual buildup of northerly flow adjacent to the coast and in the warm anomaly area (indicated by the box) during spring, but Figure 2 shows this was not the case in 1997. For example, the winds over the warm anomaly were mostly southerly during May, a result of a synoptic scale cyclonic circulation to the northwest of the warm anomaly (Figures 2b,d, and e), and the windspeed was very weak during the period from April 27 through May 10th. The northerlies finally began to intensify during the first two weeks of June, concurrent with the weakening of the warm anomaly. The existence of southerly flow during May and early June is consistent with the results of Liu et al (1998), who showed that these southerly winds were also associated with an increase in near surface specific humidity.

For the purpose of calculating area averaged quantities and computing an energy budget, we define a box (see Figure 2) with corners at (27N,126W), (40N,144W), (27N,144W) and (40N,126W) that encompasses the majority of the warm anomaly during its eastward march in April and May. Figure 3 shows the area averaged weekly SST anomaly for this box from Jan. 1982 to August 1997, and illustrates two important points. First, the warm anomaly during April and May 1997 was far more intense than any other warm anomaly occurring in the box during the nearly 16 years shown. Secondly, the warm anomaly appeared on top of a preexisting longer term anomaly or upward trend in SST. We focus our attention on the short term transient rather than the longer term upward trend in SST that was already underway.

The total, seasonal, and anomalous ocean temperature averaged over the warm anomaly area for

depths ranging from 10 to 50m is shown in figure 4. These plots are made using the NCEP weekly analyses for the first 6 months of 1997 and monthly analyses for 1980-1996. Figure 4c shows that the temperature anomaly first began to intensify in the second week of April, with the most rapid increase occurring in the surface (10m) layer. The temperature anomaly then generally increased in all layers until the second to last week of May, after which a sharp dropoff occurred until the end of June.

Figure 4a shows that the upper 20 m of the ocean remained well mixed throughout April, May, and June, with the top 50 m well mixed prior to April. From early April through the end of May, the upper 20m of water warmed more rapidly than the next 30m, resulting in a stratified boundary layer. Such a transition is typical for this time of year, as shown by the seasonal plot in 4b, but is only half as strong as the observed stratification in 1997 (Figure 4a). The subsequent weakening of the temperature anomaly returned stratification to its seasonal value by the beginning of July. Note that although the SST anomaly reached a peak of over  $2^{\circ}$  K in late April, the bulk of the anomalous warming in the top 50m of ocean actually occurred in May (Figure 4c).

The increased stratification of the top 50 m, combined with the more rapid temperature increase in the uppermost layers, suggests that warming occurred primarily from above, with the input of heat to the ocean occurring through the surface. Also, the simultaneous transition to a poorly mixed upper layer indicates that the primary mixing mechanism weakened as the total heat flux increased. One plausible explanation is that surface wind speed decreased, thereby weakening the mechanical stirring of the mixed layer while decreasing the latent and sensible heat fluxes out of the ocean. Weakened mixing would cause less dilution of the surface water by cooler water from below the surface, thereby accentuating the SST anomaly. Note that a simultaneous increase in surface specific humidity such as observed by Liu et al [1998] would decrease evaporative cooling even further and lead to an even larger SST anomaly.



## 4 Energy Considerations

We seek to identify the source of energy responsible for the warming shown in Figure 4c using the balance equation for heat content per unit area ( $Q$ ):

$$\frac{\partial Q}{\partial t} = F_l + F_s + F_{sw} - F_{lw} + F_{ek} + F_{ekp} + R_{AD} \quad (1)$$

where  $F_{sw}$  and  $F_{lw}$  are the area averaged net shortwave and longwave radiative fluxes at the ocean surface ( $F_{sw}$  is taken as positive if it is into the surface, and  $F_{lw}$  is taken as positive if it is out of the surface),  $F_l$  and  $F_s$  are the area averaged latent and sensible heat fluxes,  $F_{ek}$  ( $F_{ekp}$ ) is the area averaged horizontal (vertical) advection by Ekman currents, and  $R_{AD}$  is a residual term that includes the import or export of heat by non-Ekman current advection and diffusion. The heat energy per unit (ocean surface) area of a volume  $V_{ol}$  is

$$Q = Q_T/A, \quad (2)$$

where  $A$  is the total area of the air-sea interface of  $V_{ol}$  and  $Q_T$  is the total heat content of  $V_{ol}$ . We will see presently that it is preferable to split (1) into seasonal and anomalous parts, with the seasonal part of a variable  $\chi$  calculated for the  $i^{th}$  week (or month) of the year using

$$\chi_i^{seasonal} = \frac{\sum_{j=1}^n \chi_i^j}{n} \quad (3)$$

where  $n$  is the number of years of data available for  $\chi$ . Anomalous values of  $\chi$  are computed by subtracting the seasonal value of  $\chi$  as given by (3) from the total (also referred to as “actual”) value of  $\chi$ .

Figure 5 shows the total and seasonal  $Q$  and  $\frac{\partial Q}{\partial t}$  for the top 50 m of the warm anomaly area for January-July 1997, based on the NCEP weekly ocean analyses. The seasonal  $Q$ , computed from

the 1980-1997 NCEP monthly analyses, was sampled at weekly intervals and then smoothed using a Gaussian smoother with half width of 7 weeks and smoothing window of 30 weeks. The seasonal  $\frac{\partial Q}{\partial t}$  shown in this figure was then computed using centered time differences of the smoothed weekly-resolution  $Q$ . Figure 5 readily demonstrates the existence of anomalously warm water prior to April 1997 (note that the total heat is larger than the seasonal values in January-March), as well as the anomalous April and May warming, and shows a significant seasonal warming during April and May. Because the seasonal trend in  $Q$  is considerable, we will split (1) into seasonal and anomalous parts and analyze these separately.

#### 4.1 Latent and Sensible Heat Flux

We start our evaluation of (1) by calculating the monthly latent heat flux  $F_L$  averaged over the warm anomaly area using the bulk aerodynamic formula

$$F_L = C_d L \rho V (q_{air} - q_{sst}) \quad (4)$$

where the drag coefficient  $C_d$  is given by Smith [1980], and  $L$ ,  $\rho$ ,  $V$ ,  $q_{air}$ , and  $q_{sst}$  are the latent heat of vaporization, air density, surface wind speed, and specific humidities of surface air and air saturated at temperature equal to the SST. We use the formula of Liu [1986] in combination with SSMI column water vapor ( $C_{wv}$ ) to compute  $q_{air}$ . Since Liu's  $q_{air}$  equation works only for monthly or longer time scales, we restrict our latent heat flux calculations to monthly values, and hence must do likewise for all the forcing terms in (1). For wind speed, we use the monthly averaged SSMI surface wind speed for 1988-1996, and monthly averaged NSCAT surface wind for 1997. Seasonal and anomalous  $F_L$  are listed in tables 1 and 2, respectively. The sensible heat flux  $F_S$  is also computed using the bulk aerodynamic formula, but the resulting flux is an order of magnitude smaller than  $F_L$  (Tables 1,2), and is discussed no further.

Although of little consequence in April, the anomalous  $F_L$  accounted for a majority of the heating and cooling that occurred in May and June (Table 2). Note that using only ECMWF or SSMI winds when computing  $F_L$  produces qualitatively similar results to those obtained using NSCAT winds (ex. 15 and 19  $\text{W/m}^2$ , respectively, in May; -19 and -23  $\text{W/m}^2$  in June). Figure 6 shows  $F_L$  for 1997, along with the monthly averaged NSCAT surface winds. Figure 6 shows that  $F_L$  is significantly modulated by the surface wind speed, and that evaporative cooling of the ocean dropped considerably during May before rebounding in June. Separate calculations indicate that anomalous area-averaged  $q_{air}$  reached about 2 g/kg in May, though this was partially offset in (4) by an area-averaged anomalous  $q_{sst}$  of  $\sim 1$  g/kg. Thus the anomalous warming by  $F_L$  in May resulted from both a decrease in surface wind speed and the introduction of anomalously moist air to the warm anomaly area. Examination of Figure 2 shows that the surface winds were generally from the south during May, indicating that the moist air had its origin in the tropics, consistent with Liu et al [1998].

## 4.2 Computation of the Shortwave (SW) and Long Wave (LW) Surface Fluxes

The net radiative flux at the ocean surface is of particular interest since subjective examination of GOES-9 visible and infrared imagery from May 1997 indicates an unusually low fractional cloudiness at that time. The clouds in this area are primarily marine stratus (Warren et al [1988]) whose fractional cloudiness tends to decrease as SST increases (Bretherton and Wyant [1997], Klein et al [1995], Wyant et al [1997]). This normally happens as the stratus are advected southward, but may have occurred more rapidly in 1997 due to the warmer SST. If so, the decrease in fractional cloudiness would enhance the net radiative flux into the ocean (Norris and Leovy [1994]), and might produce an SST enhancing positive feedback between increasing SST, decreasing cloudiness, and increasing radiative flux (Klein et al [1995], Ronca and Battisti [1997], Deser and Timlin [1997]).

In order to objectively determine the fractional cloudiness, we use the one degree resolution monthly averaged  $C_{fr}$  produced by the National Climatic Data Center (NCDC), which they compute using SSM/I data and the algorithm described by Weng et al [1997]. Table 3 shows the results of averaging this  $C_{fr}$  over the warm anomaly area for April-June 1997, as well as the seasonal averages for each month based on the years 1988-1997 (excluding 1991). While the April and June values of  $C_{fr}$  are very close to their seasonal values, the May value of 0.38 is considerably lower than the seasonal value of 0.50, confirming the impression left by the GOES-9 images. If the area over which the  $C_{fr}$  is averaged is reduced to include only that area covered by the warm anomaly during May, then the  $C_{fr}$  drops to 0.22, with a seasonal value of 0.45.

Lacking direct measurements of  $F_R$ , we use version 3 of the Community Climate Model (CCM3) Column Radiation Model (CRM) to estimate the anomalous  $F_R$  for April, May, and June. The CCM3-CRM is a stand-alone one-dimensional version of the CCM3 radiation code that includes mixed phase cloud particles, pressure dependent water droplet and ice particle size, as well as trace gas and aerosol physics; more details regarding this model can be found in Kiehl et al [1996]. The CCM3-CRM requires vertical profiles of temperature and water vapor, for which we use area and monthly averaged NCEP atmospheric analyses. Vertical profiles of  $C_{fr}$  and LWP are also needed. Since the  $C_{fr}$  data in table 3 is for total cloudiness independent of height, we use the seasonally averaged  $C_{fr}$  for different cloud types presented in Warren et al [1988] to determine how the  $C_{fr}$  should be vertically distributed. Based on Warren et al [1988], we distribute the clouds among the three most common types: marine (low level) stratus, altostratus, and cirrus, with the bulk of the clouds being marine stratus. We then use previous studies to guide specification of LWP within each cloud type; details are contained in appendix A.

The results of calculating  $F_R$  for  $C_{fr}$  ranging from 0 to 1 are shown in figure 7, along with the seasonal and actual  $C_{fr}$  from table 3. In producing this plot, we have assumed that all  $C_{fr}$

variations are due to changes in marine stratus, since their seasonal  $C_{fr}$  of 0.5 is more than twice that of either the altostratus ( $C_{fr}=0.22$ ) or cirrus clouds ( $C_{fr}=0.12$ ) (Warren [1988]). The  $C_{fr}$  for the cirrus and altostratus clouds is fixed at their seasonal values. From figure 7, we determine that an anomalous  $C_{fr}$  of -0.12 during May would result in an anomalous  $F_R$  of 14 W/m<sup>2</sup>; smaller values result for April and June (see table 2). Note that the slope of the  $F_R$  vs  $C_{fr}$  curve is nearly constant for  $C_{fr}$  greater than 0.2, so the anomalous  $F_R$  is sensitive only to the anomalous  $C_{fr}$  and not the absolute  $C_{fr}$ . This is of interest since the seasonal  $C_{fr}$  using the a algorithm is 0.5, while seasonal climatology of  $C_{fr}$  based on COADS data is 0.7 (Warren [1988]).

The resulting anomalous  $F_R$  is sensitive to the choice of cloud parameters. For example, decreasing the LWP of the marine stratus clouds by half reduces the anomalous  $F_R$  by about half while increasing  $F_R$  by 20 W/m<sup>2</sup>. Doubling the fixed  $C_{fr}$  of the altostratus and cirrus clouds substantially decreases  $F_R$ , but reduces the anomalous  $F_R$  by only 2 W/m<sup>2</sup>. Both the marine stratus and higher level clouds significantly modulate  $F_R$ , but variations in marine stratus cloud parameters have a much greater effect on *anomalous*  $F_R$ . We also note that the resulting anomalous  $F_R$  is comparable to that obtained following Norris and Leovy (1994), who concluded from a number of observational data sets that a 1 % decrease in marine stratus  $C_{fr}$  should produce an increase in  $F_R$  of about 1 W/m<sup>2</sup>.

We next compare the preceding CCM3-CRM results for seasonal  $F_R$  with the Oberhuber [1988] COADS  $F_R$  climatology for May, seen together in Table 4. The Oberhuber  $F_R$  for May is less than the CCM3-CRM  $F_R$  by 35 W/m<sup>2</sup>, mostly because the Oberhuber  $F_{LW}$  is larger by 40 W/m<sup>2</sup>. It is difficult to determine the reason for these differences since the Oberhuber results were computed using simple parameterizations and a different data set. Differences in  $F_{SW}$  are small and can be eliminated by modifying the LWP of the altostratus and cirrus clouds, or by increasing their  $C_{fr}$ . There are numerous possibilities for why  $F_{LW}$  computed by the CCM3-CRM is smaller. The most

likely is misspecification of the low level  $C_{fr}$  and LWP, or differences in boundary layer water vapor. Errors in the Oberhuber climatology may also contribute (Weare [1989]), but alone probably do not explain the difference with our calculations. Since the CCM3-CRM computed  $F_{LW}$  is only weakly dependent on  $C_{fr}$  for the range of  $C_{fr}$  values examined (0.38 to 0.70), we assume the anomalous  $F_R$  is also affected only weakly.

### 4.3 Advective Terms

Proper calculation of the lateral and vertical heat advection using the NCEP ocean analyses requires that those terms be computed at each model time step during production of the analyses; a significant residual in the mass budget precludes accurate accounting of the heat budget using weekly or monthly averaged data (M. Ji, personal communication, 1998). Lacking ready access to NCEP data with timestep resolution, we instead use the NSCAT surface winds to determine the wind driven (Ekman) portion of the lateral and vertical heat advection. Advection by pressure driven currents is left as part of the residual  $R_{AD}$  in (1).

We compute the Ekman current temperature advection per unit area  $F_{ek}$  in the warm anomaly area using

$$F_{ek} = (1/A) \int_{x,y} \rho C_p (u_{ek} \frac{\partial \langle T \rangle}{\partial x} + v_{ek} \frac{\partial \langle T \rangle}{\partial y}) z_{ek} dx dy \quad (5)$$

where  $z_{ek}$  is the Ekman layer thickness,  $A$  is the horizontal area of the warm anomaly region,  $\rho$  is the water density,  $(u_{ek}, v_{ek})$  are the vertically averaged components of the Ekman current, and  $\langle T \rangle$  is the temperature vertically averaged over the depth  $z_{ek}$ . We estimate the vertical advection by Ekman pumping into the volume  $V_{ol}$  as

$$F_{ekp} = \rho C_p \int_{x,y} w_{ek} \frac{\partial T}{\partial z} \Big|_{50m} dx dy \quad (6)$$

where  $\frac{\partial T}{\partial z}\bigg|_{50m}$  is computed using centered differences over the two adjacent layers. Use of (6) gives values of  $F_{ekp}$  of 1 W/m<sup>2</sup> or less, so we ignore this term in the following discussion.

The total and seasonal values of  $F_{ek}$  determined using (5) are listed in Table 1, while the anomalous values of  $F_{ek}$ , computed by subtracting the 1992-1997 seasonally averaged  $F_{ek}$  for each month, are listed in Table 2. The magnitude of the contribution from anomalous  $F_{ek}$  to (1) is essentially zero for April and May, and only -4 W/m<sup>2</sup> in June. While it is clear that  $F_{ek}$  contributed little to the overall area averaged energy balance, the spatial distribution of  $F_{ek}$  (not shown) was nonuniform, with values of  $F_{ek}$  of -5 to -20 W/m<sup>2</sup> on the west side of the warm anomaly during May. During this time the warm anomaly generally moved eastward, leaving open the possibility that the Ekman advection assisted in that propagation by suppressing the warm anomaly in the west.

## 5 Errors and Overall Results

The seasonal and 1997 overall energy budget (table 1) is dominated by the net radiative heating  $F_R$  and, to a lesser extent, evaporative cooling ( $F_L$ ). Note that the calculated combined net forcings for both seasonal and 1997 are consistently higher than the observed net forcing  $\frac{\partial Q}{\partial t}$  by 20-70 W/m<sup>2</sup>. Based on the comparison of radiative fluxes with the Oberhuber climatology, as much as 40 W/m<sup>2</sup> of this difference results from  $F_{LW}$  that is too small in our calculations. The remainder could result, as we will see presently, from errors in the latent heat flux and other forcing terms.

Table 2 summarizes the anomalous energy budget calculations, with the addition of the time rate of change of  $Q$  and error estimates for April, May, and June. Estimating error for parameterized calculations of poorly measured quantities such as  $F_L$  and  $F_S$  is difficult at best, but an attempt is nevertheless made in hope of highlighting sources of error and approximate magnitudes of errors.

We first consider errors in  $Q$ , which result mainly from uncertainty in the subsurface temperature; we assume salinity errors are negligible. Ji et al [1995] estimate the error in the NCEP subsurface

temperature data to be no better than 0.3 K. The variations in subsurface temperature through April and May range from as much as 3 degrees for the upper two layers, to as little as 1 K for the lowest layer. We calculate the percentage error  $E$  in the temperature variations, and hence in  $Q$ , using:

$$E = \sum_{i=1,5} (\varepsilon_i \delta_{z_i} / T'_i) / \sum_{i=1,5} \delta_{z_i} \quad (7)$$

where

$$\varepsilon_i = 0.3^\circ\text{C}$$

$$\delta_{z_i} = \text{layer thickness (10m)}$$

$$T'_i = \text{monthly temperature variation}$$

Using (7) with the observed  $T'_i$  gives a percentage error of  $\sim 15\%$  for  $Q$ , a result that is based on the assumption that the errors are random and not systematic. Area averaging the  $1^\circ$  grid temperatures probably reduces the error in  $Q$ , and we assume that this offsets the fact that  $\varepsilon = 0.3\text{K}$  is a *minimum* estimate.

Although some error in  $F_L$  results from uncertainty in the input data used in (4), the bulk of the error results from deficiency in (4) itself. Since  $F_L$  is so difficult to measure directly, the limitations in (4) are not easily quantified, though the wide range of values used for  $C_d$  over the years suggest an uncertainty of 50% or more in  $F_L$  is possible, especially at very low and very high wind speeds [Blanc 1985]. We assume then that the error in the  $F_L$  is 50% of the larger of the seasonal and actual  $F_L$  for a given month, giving error of 29, 25, and 38  $\text{W/m}^2$  for April, May, and June respectively. We likewise assign 50% error to  $F_S$ , though it has a much smaller effect on the overall heat budget.

We have seen that the anomalous  $F_R$  is insensitive to choice of the seasonal and actual  $C_{fr}$ , so long as the anomalous  $C_{fr}$  remains fixed. There is also only weak sensitivity of anomalous  $F_R$  to



the choice of the fixed  $C_{fr}$  and LWP for the altostratus and cirrus clouds. Thus we assume that the error in  $F_R$  results from errors in the  $C_{fr}$  anomaly and in the LWP of the marine stratus clouds. Weng et al [1997] compare their  $C_{fr}$  with the ISCCP  $C_{fr}$  ( $C_{fr}^{ISCCP}$ ) for November 1987, and discuss deficiencies in both. Since there is uncertainty in both the Weng and the ISCCP  $C_{fr}$ , we assume that the amount of scatter in  $C_{fr}^{ISCCP}$  for a given value of  $C_{fr}^{SSMI}$  shown in Figure 4a of Weng et al [1997] is indicative of the amount of random error in  $C_{fr}^{SSMI}$  for an individual gridpoint. This results in an error of about 15 % in the individual gridpoint  $C_{fr}$ , which shrinks to about 3 % when the  $C_{fr}$  is averaged over the warm anomaly area. Additional error is produced by assuming that the stratus cloud LWP is fixed at the values found from Blaskovic et al [1991], whose study used data taken from a single location. Stratus clouds are sensitive to SST, surface wind speed, and other local meteorological parameters that vary considerably over the warm anomaly area. Though we lack specific data regarding how LWP would vary, it is not unreasonable to assume an error of 25 % in the LWP, which would translate into a similar error in the anomalous  $F_R$ , much larger than the 3 %  $C_{fr}$  error. Hence we take 25 % of the anomalous  $F_R$  as the amount of error in that variable.

Finally, the error in the Ekman advection calculation results primarily from uncertainty in the wind speed,  $\langle T \rangle$ , and  $C_d$ , the combination of which result in an error of 1-2 W/m<sup>2</sup> of the area averaged  $F_{ek}$ . The error in the Ekman pumping calculation is O(100%), but the contribution from this term is still negligible, and so ignored.

Referring to Table 2, we see that during April, the combined anomalous surface fluxes ( $F_{NS}$ ,  $F_{NS} = F_L + F_S + F_R$ ) amounted to +7 W/m<sup>2</sup>, 33% of the 21 W/m<sup>2</sup> needed to account for the observed warming. The error bars on  $F_{NS}$  are large enough so that  $F_{NS}$  could account for the warming, especially if the observed warming was overestimated. In May, when the bulk of the warming took place,  $F_{NS}$  easily accounts for the observed warming, with anomalous latent and radiative heating accounting for the bulk of the warming. The large role played by anomalous  $F_L$

is consistent with the results of Liu et al. (1998), as is the role of the anomalously high  $q_{air}$  in suppressing  $F_L$ . The  $F_L$  was also suppressed by the anomalously low wind speed, highlighting the fact that surface wind direction and magnitude both play important roles in modulating  $F_L$  and  $F_S$ . In addition, the decrease in cloudiness created a substantial increase in the radiative warming of the water, without which the SST anomaly could not have reached its extreme intensity.

In June, when the SST anomaly shrunk in size and weakened in intensity, the anomalous latent and sensible heating became negative, with comparable magnitudes to their May values. This anomalous cooling occurred both because the wind became stronger and because it became more northerly, ending the advection of moist tropical air into the warm anomaly area. And although the monthly averaged  $q_{air}$  dropped in June, the monthly averaged SST anomaly was nearly the same as in May, resulting in a positive  $q_{sst}$  anomaly which, with the lower  $q_{air}$ , further enhanced the evaporative cooling. The area averaged  $C_{fr}$  returned to normal in June, so the radiative warming anomaly was small. The error bars on  $F_{NS}$  and the observed cooling are large enough for some overlap between  $F_{NS}$  and  $\frac{\partial Q}{\partial t}$ . The large residual leaves open the possibility that advection by geostrophic currents may have made a significant contribution to (1) during June.

## 6 Discussion

We have shown that anomalously large  $F_L$  and  $F_R$  accounted for the bulk of the warming during May, while anomalously small  $F_L$  weakened the warm anomaly in June. The radiative warming was of secondary importance in that it accentuated, but did not control, the warming transient. Any positive feedback between  $C_{fr}$ , SST, and  $F_R$  was overwhelmed by variations of surface wind speed and  $F_L$ . Since the variation of the surface wind speed and direction played a pivotal role in the formation and dissolution of the warm anomaly, we investigate surface winds by examining the 1000 mb geopotential height fields, keeping in mind that the surface winds themselves are nongeostrophic.

Typically, the North Pacific subtropical high is evident in monthly average geopotential height ( $Z$ ) maps as early as March, and establishes a northeasterly flow in the warm anomaly area as it strengthens through April and May. This was not the case in 1997, as indicated by Figure 8. Figure 8a shows the NCEP monthly averaged 1000 mb  $Z$  ( $Z_{1000}$ ) for May 1997, while Figure 8b shows the long term (1979-1995) NCEP mean for  $Z_{1000}$  in May. The subtropical high east of 150W almost disappeared in May 1997, mostly because of the appearance of a cutoff low centered near 135 W, 40N around the 10th of May. This cutoff low drifted eastward for about 1 week until it reached the west coast of the U.S., and then drifted southward and westward before combining with another cutoff low near 170W, 40N on May 22. The resulting low pressure system moved northward and continued to disrupt the formation of the subtropical high through the end of May. The deterioration of the subtropical high eliminated the normally steady surface northeasterlys, resulting in the weaker southerly winds shown in Figure 2.

Figure 8 demonstrates that the change in surface winds in the warm anomaly area resulted from variations in synoptic and planetary scale circulations. In particular, pressure in the warm anomaly area during May is typically much higher than in the Gulf of Alaska, as demonstrated by Figures 9a and 9b. To construct these figures, we first calculated the monthly  $Z_{1000}$  averaged over the warm anomaly region and then over a similarly sized region centered in the Gulf of Alaska for each year from 1979 to 1997 using NCEP analyses (see boxes in Figure 8). We then computed the ratio  $Z_{1000}^{wa}/Z_{1000}^{ga}$  ( $wa$  = warm anomaly,  $ga$  = Gulf of Alaska) and plotted it in Figure 9b. In nearly every case, high pressure dominated in the warm anomaly area and low pressure in the Gulf of Alaska, resulting in a relatively large value for  $Z_{1000}^{wa}/Z_{1000}^{ga}$ . The notable exception is 1997, when low pressure dominated in both areas, resulting in a much smaller value of  $Z_{1000}^{wa}/Z_{1000}^{ga}$ . The ratio  $Z_{1000}^{wa}/Z_{1000}^{ga}$  was also nearly 1 during 1996, though the pressure in the warm anomaly area was not as low as in May 1997.

Finally, we note that the resulting distribution of  $Z_{1000}$  and surface winds, along with the subsequent decrease in surface latent heat flux and rise in SST, is similar to the sequence of events modeled by Alexander [1992a,b], Lau and Nath [1994], and others for the mature phase of El Niño. The primary difference is that, in the case studied here, El Niño was just beginning and the season was spring, not winter. Furthermore, the SST anomaly was already in place before El Niño began, and the spatial structure did not change significantly during the intensification or weakening phase. Given this evidence, it seems unlikely that El Niño directly triggered the formation of the warm anomaly. A more likely scenario is that a third and separate atmospheric event triggered both El Niño and the warm anomaly.

The tropical Intraseasonal Oscillation (ISO) or 30-60 day wave might serve as such a trigger. During its mature phase, the eastward propagating ISO often produces equatorial westerly wind bursts in the western and central equatorial Pacific, creating eastward propagating Kelvin waves with the potential to influence eastern Pacific SST (ex, McPhaden et al [1988]). In addition, theoretical and modeling studies have shown that the anomalous heating associated with the ISO can produce extratropical response in the form of persistent 500 mb geopotential height anomalies in the north Pacific (ex. Higgins and Schubert, [1996]). Higgins and Schubert's results indicate that the anomalous convective heating associated with the ISO can initiate midlatitude circulation anomalies within 6-10 days, and that the subsequent growth of the circulation anomaly draws on the basic state flow for energy. During March 1997, a strong westerly wind burst occurred that extended as far east as 170W, and triggered an eastward propagating Kelvin wave which preliminary results indicate was at least partly responsible for the April warming off the coast of Peru [Liu et al 1998]. If this wind burst originated from the ISO, then the anomalous convective heating associated with the ISO (or perhaps with following ISO events in April) may have concurrently forced a change in the North Pacific 500 mb height field related to the unusual  $Z_{1000}$  variability in the warm anomaly

area. Another possibility is that the near simultaneous appearance of the warm anomaly and the beginning of El Niño was a statistical coincidence. The resolution of this question awaits future research.

## Appendix A

The vertical profiles of  $C_{fr}$  and cloud liquid water path (LWP) for the marine stratus, altostratus, and cirrus clouds are required input for the CCM3-CRM. In order to provide a realistic vertical profile of the LWP for the marine stratus, we use the results of Frisch et al [1995] and Blaskovic et al [1991]. During the July 1987 FIRE experiment, Blaskovic measured the diurnal cycle of the column integrated LWP (ILWP) for marine stratus clouds using data from the NOAA surface based 3-channel microwave radiometer. To find the vertical profile of the LWP, we multiply the Blaskovic ILWP values by a normalized vertical profile of LWP computed from the LWP vertical profile results of Frisch. The Frisch LWP profile was retrieved from  $K_{alpha}$ -band doppler radar and microwave radiometer data collected during ASTEX (Atlantic Stratocumulus Transition Experiment), which took place in the vicinity of the Azores during June 1992. The stratus clouds observed during ASTEX were generally thicker and higher than those observed during FIRE, so we vertically rescaled the normalized Frisch profile to fit in a 300m thick cloud layer, roughly comparable to the FIRE marine stratus layers described by Blaskovic [1991] and Minnis et al [1992]. We made no allowance for the variability in stratus vertical thickness during the day, but did allow the ILWP to vary through the day in a manner consistent with Blaskovic's diurnal cycle. Finally, we assumed that  $C_{fr}$  is independent of height within the stratus cloud, and computed surface radiative fluxes for cases with  $C_{fr}$  varying from 0 to 1.0, at each of the local hours 6,8,10,...20 for each month.

Lacking detailed data, we specify fixed LWP for both the altostratus and cirrus clouds. The altostratus clouds lie between 600 and 700 mb with ILWP of 160 g/m<sup>2</sup>, smaller than that used by Muller et al [1994], but greater than that found in Starr and Cox [1985]. The precise value of altostratus ILWP was chosen to bring the  $F_{SW}$  into line with the results of Oberhuber [1988]. The cirrus clouds extend from 300 to 225 mb and have ILWP of 19 g/m<sup>2</sup>, and are based on the

compilation of studies presented by Liou [1986].

### **Acknowledgements**

The research described in this paper was carried out by the Jet Propulsion Laboratory, California Institute of Technology, under contract with the National Aeronautics and Space Administration. Support from the NSCAT project is acknowledged. NCAR/NCEP Reanalysis and operational analysis data was provided through the NOAA Climate Diagnostics Center (<http://www.cdc.noaa.gov/>). We would like to thank Dr. Van Snyder for producing the gridded NSCAT wind field.



## References

- Alexander, M.A., Midlatitude atmosphere-ocean interaction during El-Nino. Part I: The north pacific ocean, *J.Climate*, **5**, 944-958, 1992.
- , Midlatitude atmosphere-ocean interaction during El-Nino. Part II: The northern hemisphere atmosphere, *J.Climate*, **5**, 959-972, 1992.
- Blaskovic, M., R. Davies, and J.B. Snider, Diurnal variation of marine stratocumulus over San Nicholas island during July 1987, *Mon.Wea.Rev.*, **119**, 1469-1478, 1991.
- Bretherton, C.S., and M.C. Wyant, Moisture transport, lower-tropospheric stability, and decoupling of cloud-topped boundary layers, *J.Atmos.Sci.*, **54**, 148-167, 1997.
- Deser, C. and M.L. Blackmon, On the relationship between tropical and north pacific sea surface temperature variations, *J.Climate*, **8**, 1677-1680, 1995.
- , and M.S. Timlin, Atmosphere-ocean interaction on weekly timescales in the north Atlantic and Pacific, *J.Climate*, **10**, 393-408, 1997.
- Freilich, M.H. and R. Scott Dunbar, The accuracy of the NSCAT 1 vector winds: Comparisons with National Data Buoy Center buoys, *J.Geophys.Res.*, **104**, 11231-11246, 1999.
- Frisch, A.S., C.W. Fairall, and J.B. Snider, Measurement of stratus cloud and drizzle parameters in ASTEX with a K-alpha-band doppler radar and a microwave radiometer, *J.Atmos.Sci.*, **52**, 2788-2799, 1995.
- Higgins, R.W. and S.D. Schubert, Simulations of persistent North Pacific circulation anomalies and interhemispheric teleconnections, *J.Atmos.Sci.*, **53**, 188-207, 1996.
- Hsiung, J. and R.E. Newell, The principle nonseasonal modes of variation of global sea surface temperature, *J.Phys.Oceanogr.*, **13**, 1957-1967, 1983.

- Ji, M., A. Leetma, and J. Derber, An ocean analysis system for seasonal to interannual climate studies, *Mon.Wea.Rev.*, **123**, 460-481, 1995.
- Kiehl, J.T., J.J. Hack, G.B. Bonan, B.A. Boville, B.P. Briegleb, D.L. Williamson, and P.J. Rasch, Description of the NCAR Community Climate Model (CCM3), NCAR Technical Note 420, Boulder, CO, 1996.
- Klein, S.A., D.L. Hartmann, and J.R. Norris, On the relationships among low-cloud structure, sea surface temperature, and atmospheric circulation in the summertime northeast pacific, *J.Climate*, **8**, 1140-1155, 1995.
- Lau, N-C. and M.J. Nath, A modeling study of the relative roles of tropical and extratropical SST anomalies in the variability of the global-atmosphere system, *J.Climate*, **7**, 1184-1207, 1994.
- Liou, Kuo-Nan, Influence of cirrus clouds on weather and climate processes: A global perspective, *Mon.Wea.Rev.*, **114**, 1167-1198, 1986.
- Liu, W.T., Statistical relation between monthly mean precipitable water and surface-level humidity over global oceans, *Mon.Wea.Rev.*, **114**, 1591-1602, 1986.
- , W.Tang, and H. Hu, Spaceborne sensors observe El Nino's effects on ocean and atmosphere in North Pacific, *Eos.Trans., AGU*, **79**, 249-252, 1998.
- McPhaden, M.J., H.P. Freitag, S.P. Hayes, B.A. Taft, Z. Chen, and K. Wyrtki, The response of the equatorial Pacific ocean to a westerly windburst in May 1986, *J.Geophys.Res.*, **93**, 10589-10603, 1988.
- Minnis, P., P.W. Heck, D.F. Young, C.W. Fairall, and J.B. Snider, Stratocumulus cloud properties derived from simultaneous satellite and island-based instrumentation during FIRE, *J.Appl.Meteor.*, **31**, 317-339, 1992.

- Muller, B.M., H.E. Fuelberg, and X. Xiang, Simulations of the effects of water vapor, cloud liquid water, and ice on AMSU moisture channel brightness temperatures, *J.Appl.Meteor.*, **33**, 1133-1154, 1994.
- Norris, J.R. and C.B. Leovy, Interannual variability in stratiform cloudiness and sea surface temperature, *J.Climate*, **7**, 1915-1925, 1994.
- Oberhuber, J.M., An atlas based on the COADS data set: The budgets of heat, buoyancy and turbulent kinetic energy at the surface of the global ocean, Max-Planck-Institut fur Meteorologie, Report No. 15, Hamburg, 1988.
- Reynolds, R.W. and T.M. Smith, Improved global sea surface temperature analyses using optimal interpolation, *J.Climate*, **7**, 929-948, 1994.
- Ronca, R.E. and D.S. Battisti, Anomalous sea surface temperatures and local air-sea energy exchange on intraannual timescales in the northeastern subtropical pacific, *J.Climate*, **10**, 102-117, 1997.
- Smith, S.D., Wind stress and heat flux over the oceans in gale force winds, *J.Phys.Oceanogr.*, **10**, 709-726, 1980.
- Starr, D.O'C., and S.K. Cox, Cirrus clouds. Part II: Numerical experiments on the formation and maintenance of cirrus, *J.Atmos.Sci.*, **42**, 2682-2694, 1985.
- Warren, S.G., C.J.Hahn, J. London, R.M. Chervin, and R.L. Jenne, 1988: Global distribution of total cloud cover and cloud type amounts over the ocean, U.S. Dept. of Energy DOE/ER/60085-H1, NCAR Technical Notes NCAR/TN-317+STR, NTIS-PR-360.

- Weare, B.C., A.R. Navato, and R.E. Newell, Empirical orthogonal analysis of pacific sea surface temperatures, *J.Phys.Oceanogr.*, **15**, 671-678, 1976.
- , Uncertainties in estimates of surface heat fluxes derived from marine reports over the tropical and subtropical oceans, *Tellus*, **41A**, 357-370, 1989.
- Weng, F., N.C. Grody, R. Ferraro, A. Basist, and D. Forsyth, Cloud liquid water climatology from the special sensor microwave imager, *J.Climate*, **10**, 1086-1098, 1997.
- Wentz, F., A well-calibrated ocean algorithm for special sensor microwave/imager, *J.Geophys.Res.*, **102**, 8703-8718, 1997.
- Wyant, M.C., C.S. Bretherton, H.A. Rand, and D.E. Stevens, Numerical simulations and a conceptual model of the subtropical marine stratocumulus to trade cumulus transition. *J.Atmos.Sci.*, **54**, 168-192, 1997.

Table 1: 1997 and Seasonal Heat Budgets ( $\text{W/m}^2$ )

Heat Budget	April	May	June
Latent Heat, 1997	-55	-30	-76
seasonal	-59	-51	-56
Sensible Heat, 1997	-5	-3	-13
seasonal	-6	-7	-8
Ekman Adv (horizontal), 1997	-6	-3	-7
seasonal	-5	-3	-3
Ekman Adv (vertical), 1997	0	0	2
seasonal	0	0	1
Net Radiative, 1997	167	192	186
seasonal	164	178	185
Net Forcing, 1997	101	156	92
seasonal	93	117	121
Observed $dQ/dt$ , 1997	46	117	19
seasonal	25	63	101

Table 2: Anomalous Heat Budget ( $\text{W/m}^2$ )

Anomalous Budget	April	May	June
Latent Heat	4	21	-20
Error	29	25	38
Sensible Heat	1	4	-5
Error	3	3	6
Ekman Adv (horizontal)	-1	0	-4
Error	2	2	2
Ekman Adv (vertical)	0	0	1
Error	1	1	2
Net Radiative	3	14	1
Error	1	4	0
Net Forcing	7	39	-27
Error	36	35	48
Observed $dQ/dt$	21	54	-82
Error	3	8	12

Table 3: Monthly Averaged Cloud Fraction over  
Warm Anomaly Region

Time Period	March	April	May	June
1997	0.52	0.41	0.38	0.51
Seasonal	0.50	0.44	0.50	0.52

Table 4: Shortwave, Longwave, and Net Radiative  
Fluxes ( $\text{W/m}^2$ )

Source/Wavelength:	April	May	June
CCM3-CRM SW	177	189	193
CCM3-CRM LW	13	11	8
CCM3-CRM NET	164	178	185
Oberhuber SW	172	194	197
Oberhuber LW	54	51	46
Oberhuber NET	118	143	151

## Figure Legends

**Figure 1.** (a) First nonseasonal EOF of SST based on data from 1949-1973, reprinted from Weare et al (1976). (b) April-May 1997 average of Reynold's SST anomaly (units: degrees C). Anomaly was computed by subtracting the seasonal cycle based on 1982-1997 Reynold's SST data. (c) Same as (b), except average is for January 1996 through March 1997.

**Figure 2.** (a-i) Color contours show weekly SST anomaly (units: degrees C) for each week from April 13-19 to June 8-14, 1997. Wind socks are the actual (not anomalous) weekly averaged NSCAT surface winds, with the hooked portion representing the tail of the vector. Magnitude of wind vectors (units: m/s) is indicated by diagram inset over north-central U.S. The boxed area west of the U.S. is the region over which all area averaged quantities and the energy balance are computed, unless otherwise noted.

**Figure 3.** Weekly SST anomaly (units: degrees C) after averaging over the warm anomaly area defined by the box in Figure 2. The seasonal cycle that was removed was based on the years 1982-1997.

**Figure 4.** Weekly NCEP analyzed ocean temperatures (units: degrees C) averaged over the warm anomaly area. Temperature is shown separately for the top 5 layers (each 10m thick); solid line is for surface to 10m, dotted line is for 10m to 20m, and so on as indicated in legend. (a) Actual layer temperatures for 1997. (b) Seasonal temperatures based on 1980-1996 NCEP monthly analyses. (c) Anomalous layer temperatures for 1997 computed by subtracting the weekly sampled seasonal values from the actual 1997 weekly values.



**Figure 5.** *Black solid and green dotted lines:* Total heat per unit area ( $Q$ ; units are  $J/m^2$ ) for the top 50m of ocean in the warm anomaly area, based on NCEP ocean analyses; black line is  $Q$  for 1997, green line is the 1980-1996 seasonal value (see text for details). *Blue and Red lines:* heating rates per unit area ( $\frac{\partial Q}{\partial t}$ , units are  $W/m^2$ ) calculated from  $Q$ .

**Figure 6.** *Solid Line, left ordinate:* Monthly latent heat flux averaged over the warm anomaly area for January through June 1997 (units are  $W/m^2$ ). *Dashed Line, right ordinate:* NSCAT surface wind speed averaged over the warm anomaly region and for each month of 1997 (units are m/s).

**Figure 7.** Daily averaged shortwave (SW) radiative flux at ocean surface (solid lines) and net (NET) radiative surface flux (dashed lines) as a function of fractional cloud coverage. The seasonal and actual (1997) values of the net radiative flux are indicated by "S" and "A" on the respective curves for each month. Units are  $W/m^2$ .

**Figure 8.** (a) NCEP analyzed 1000 mb geopotential height (units: m) averaged for May 1997. Contour interval is 50m. Rectangular boxes in Gulf of Alaska and off U.S. west coast are used for computing the geopotential height index shown in Figure 9 (see text for details). (b) same as (a) except 1979-1995 NCEP mean for May is used.

**Figure 9.** (a) Geopotential height (units: m) for May only of each year from 1979 through 1997. Asterisks indicate geopotential height averaged over the Gulf of Alaska rectangle (see Figure 8), while crosses are the average over the warm anomaly rectangle in Figure 8. (b) Ratio of  $Z_{wa}$  to  $Z_{ga}$  given in (a) for each May of 1979-1997.

□)

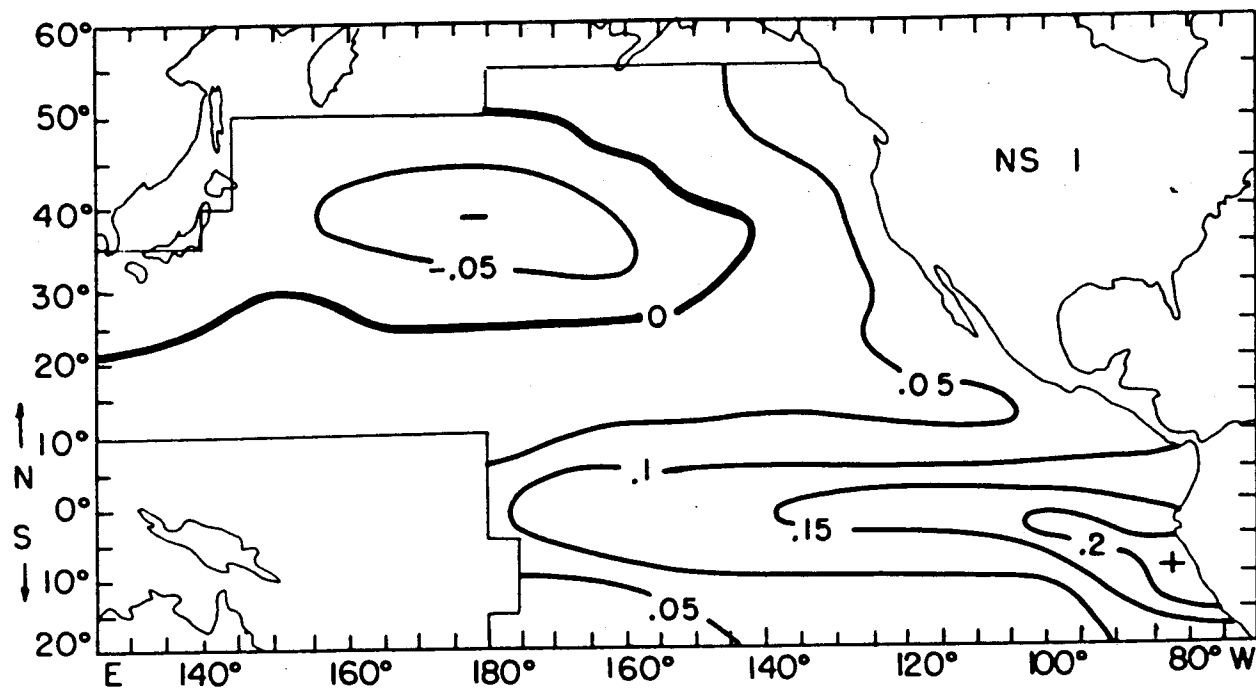
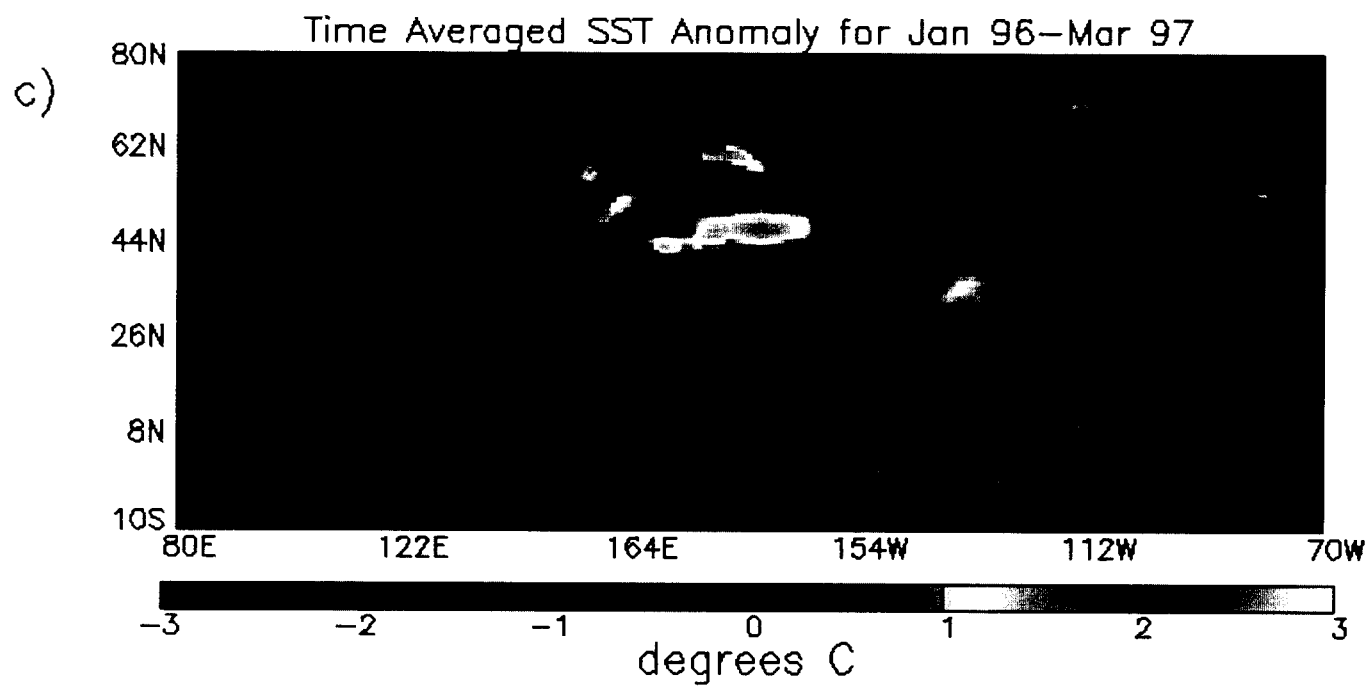
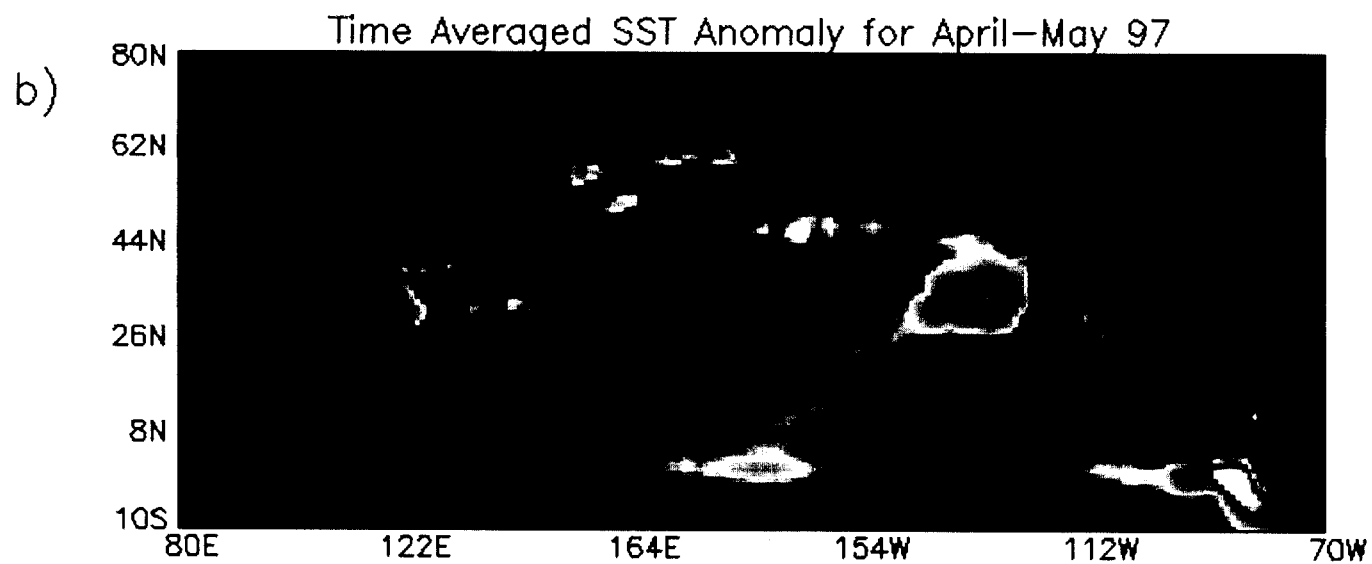
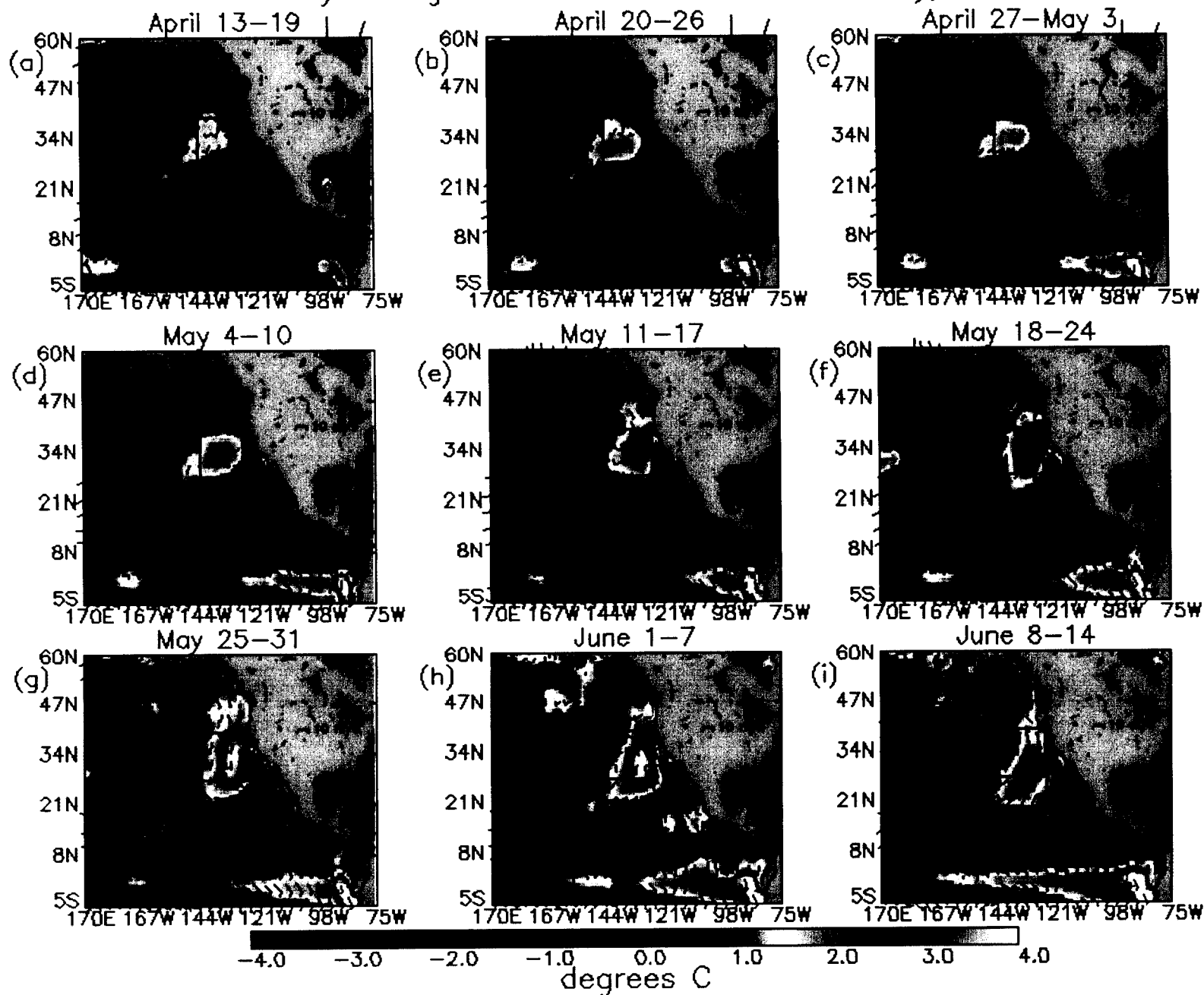


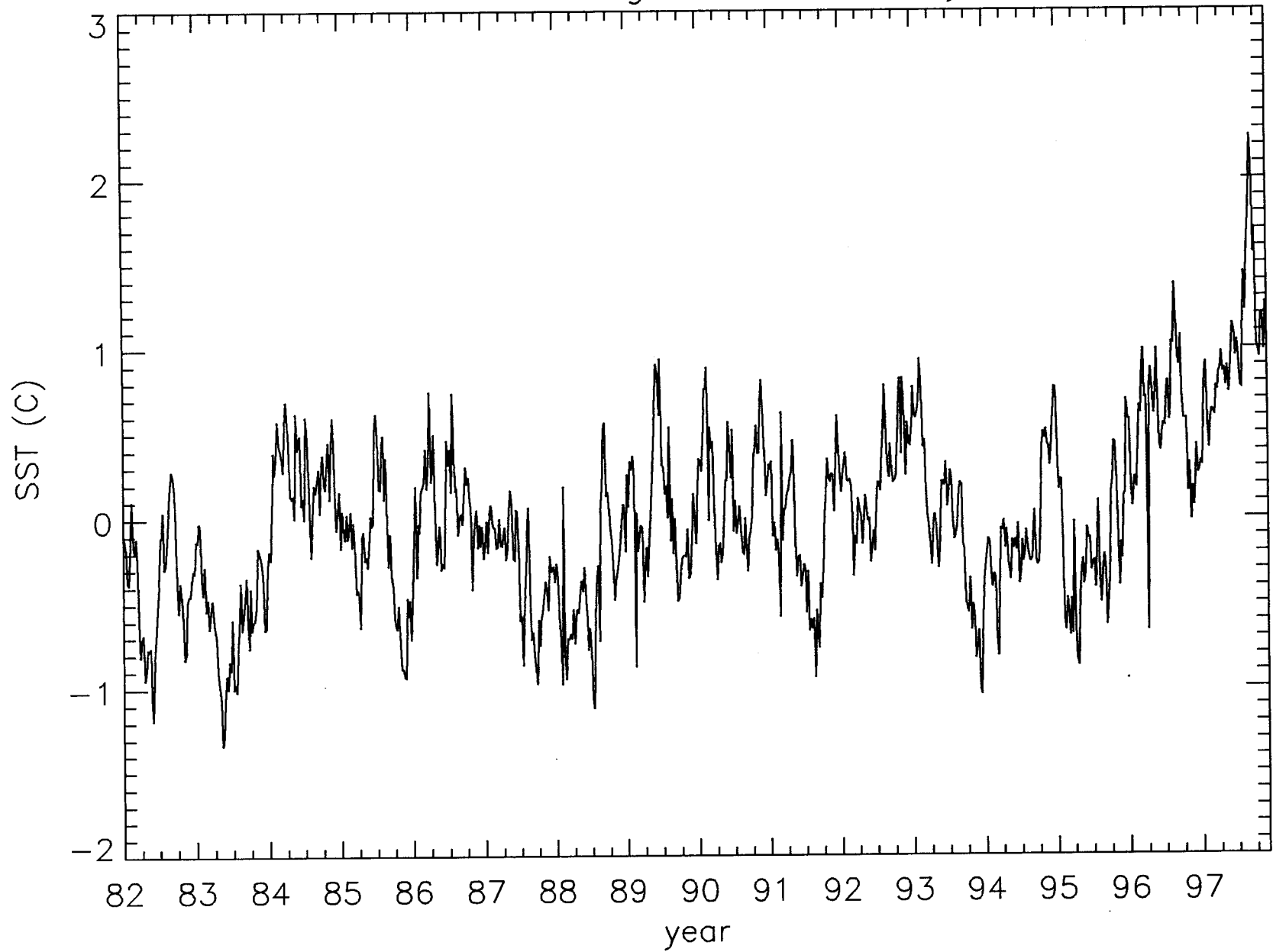
Fig. 1a



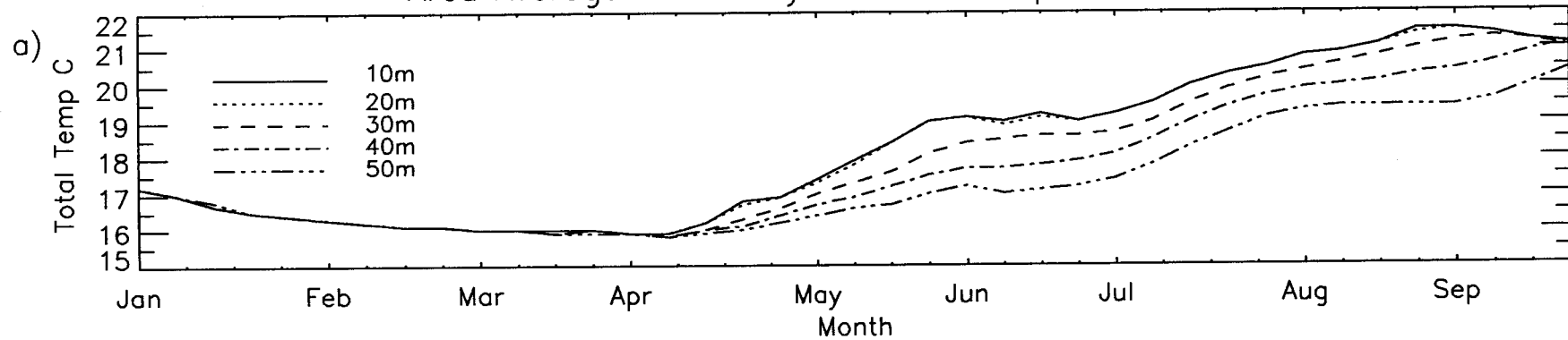
# Weekly Averaged NSCAT Winds and SST Anomaly, 1997



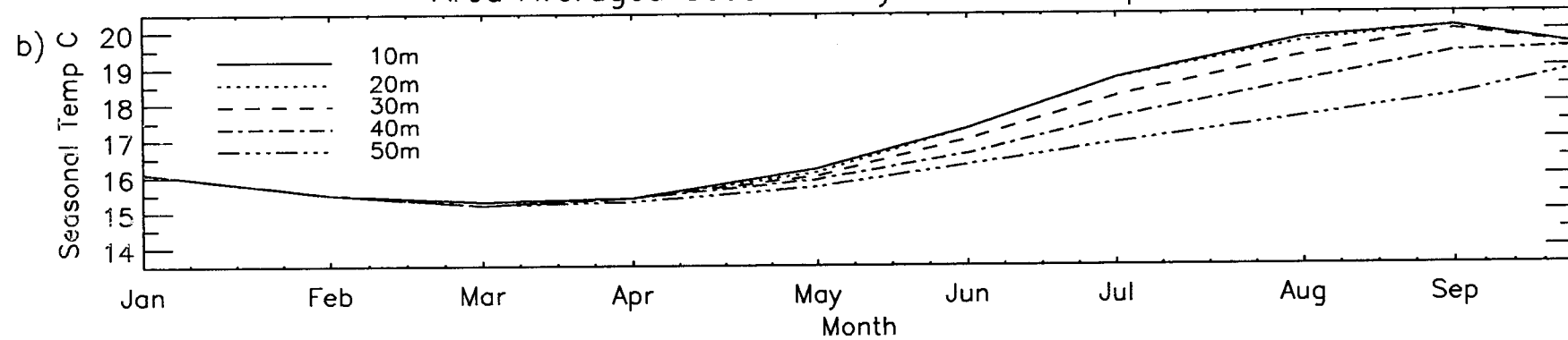
# Area Averaged SST Anomaly



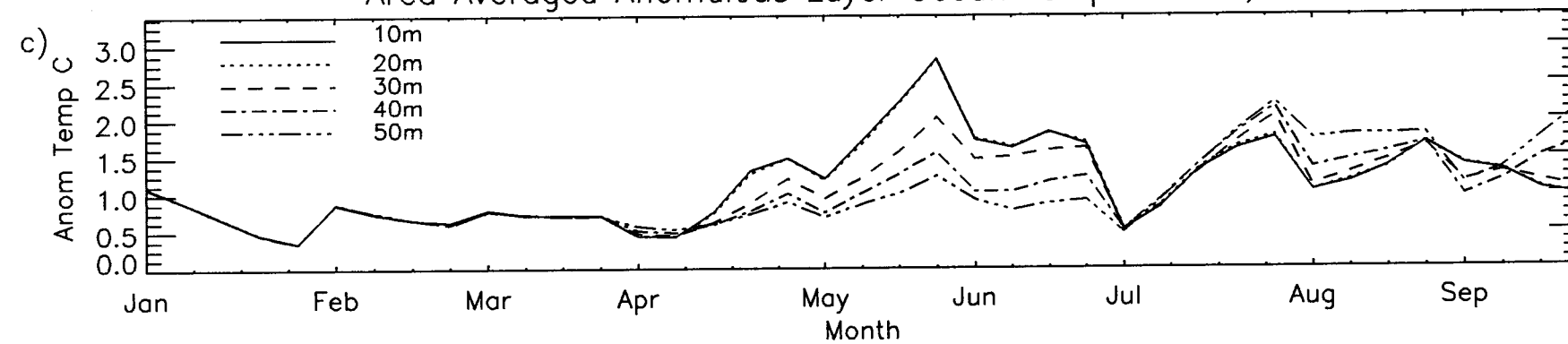
Area Averaged Total Layer Ocean Temperatures, 1997

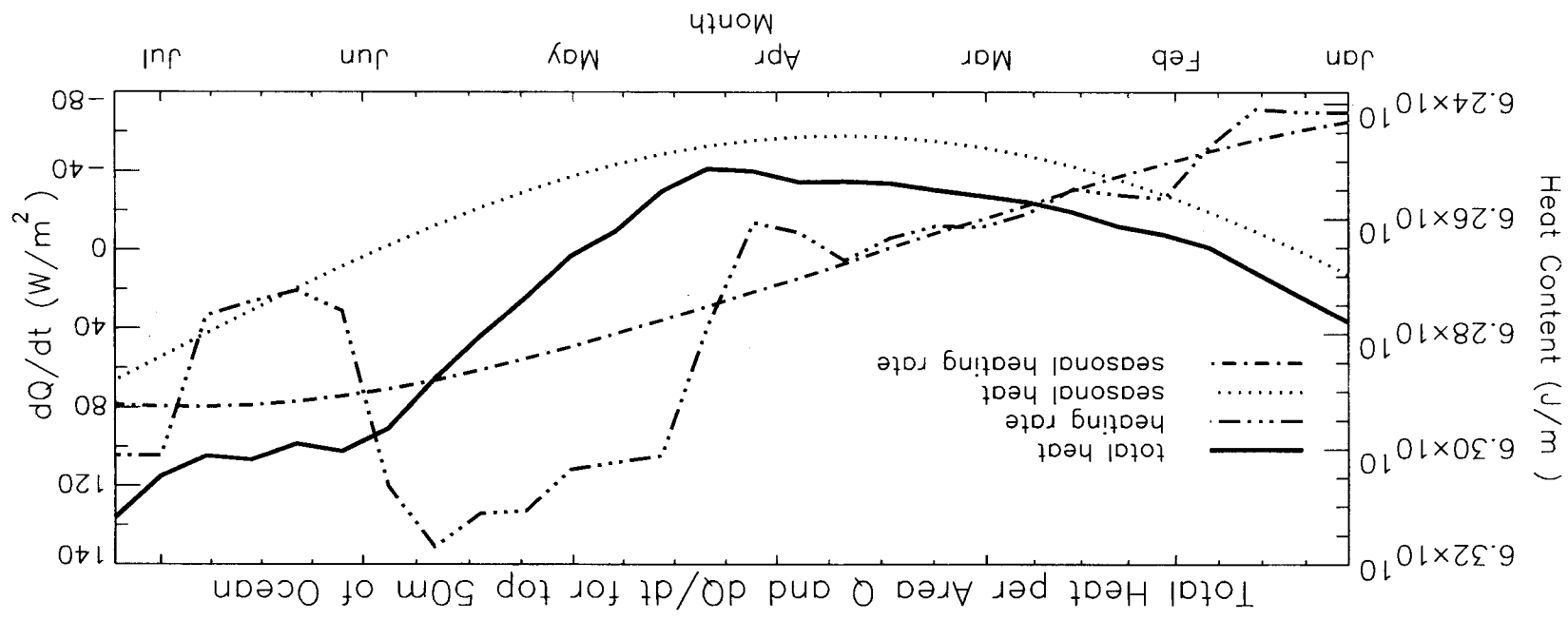


Area Averaged Seasonal Layer Ocean Temperatures

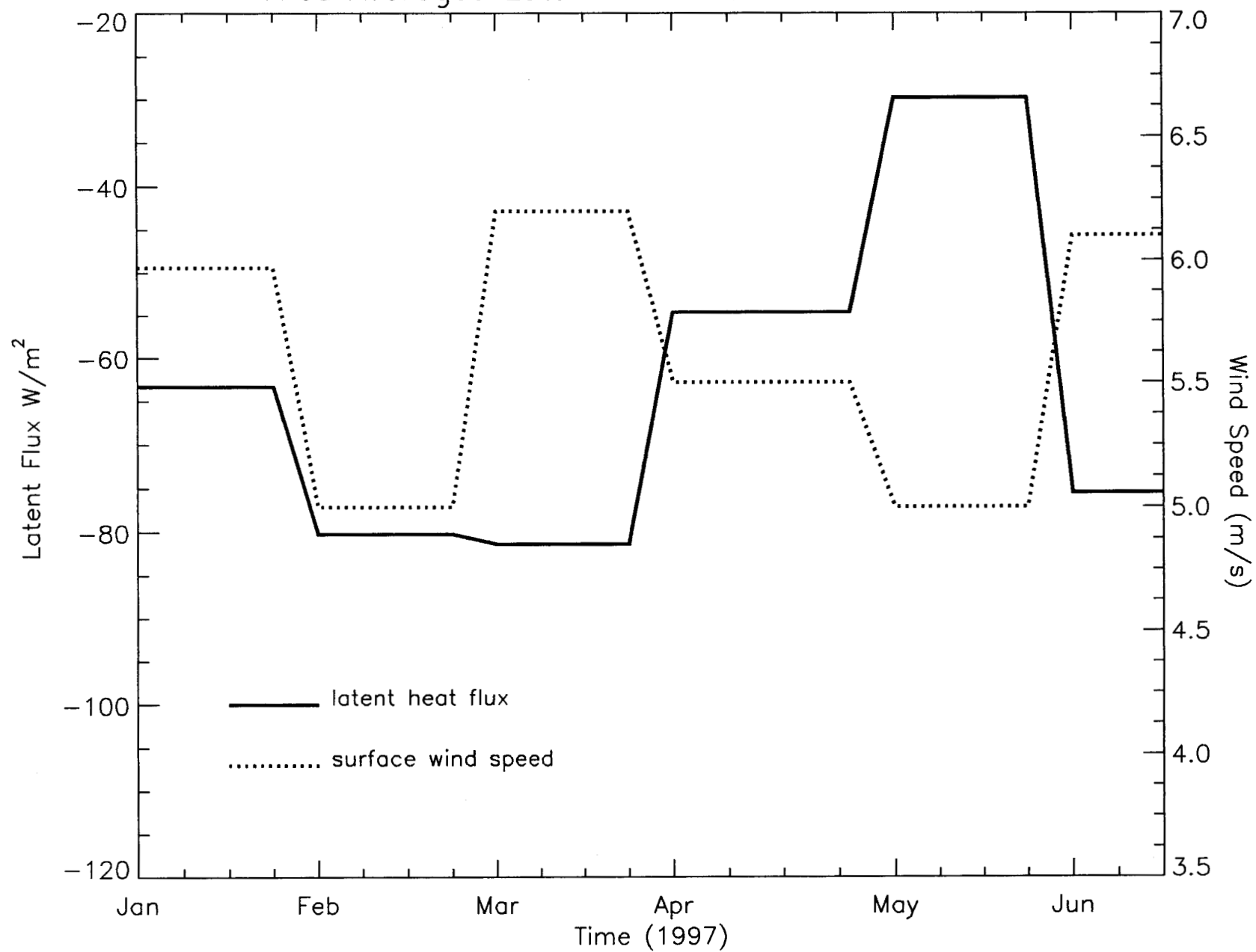


Area Averaged Anomalous Layer Ocean Temperatures, 1997



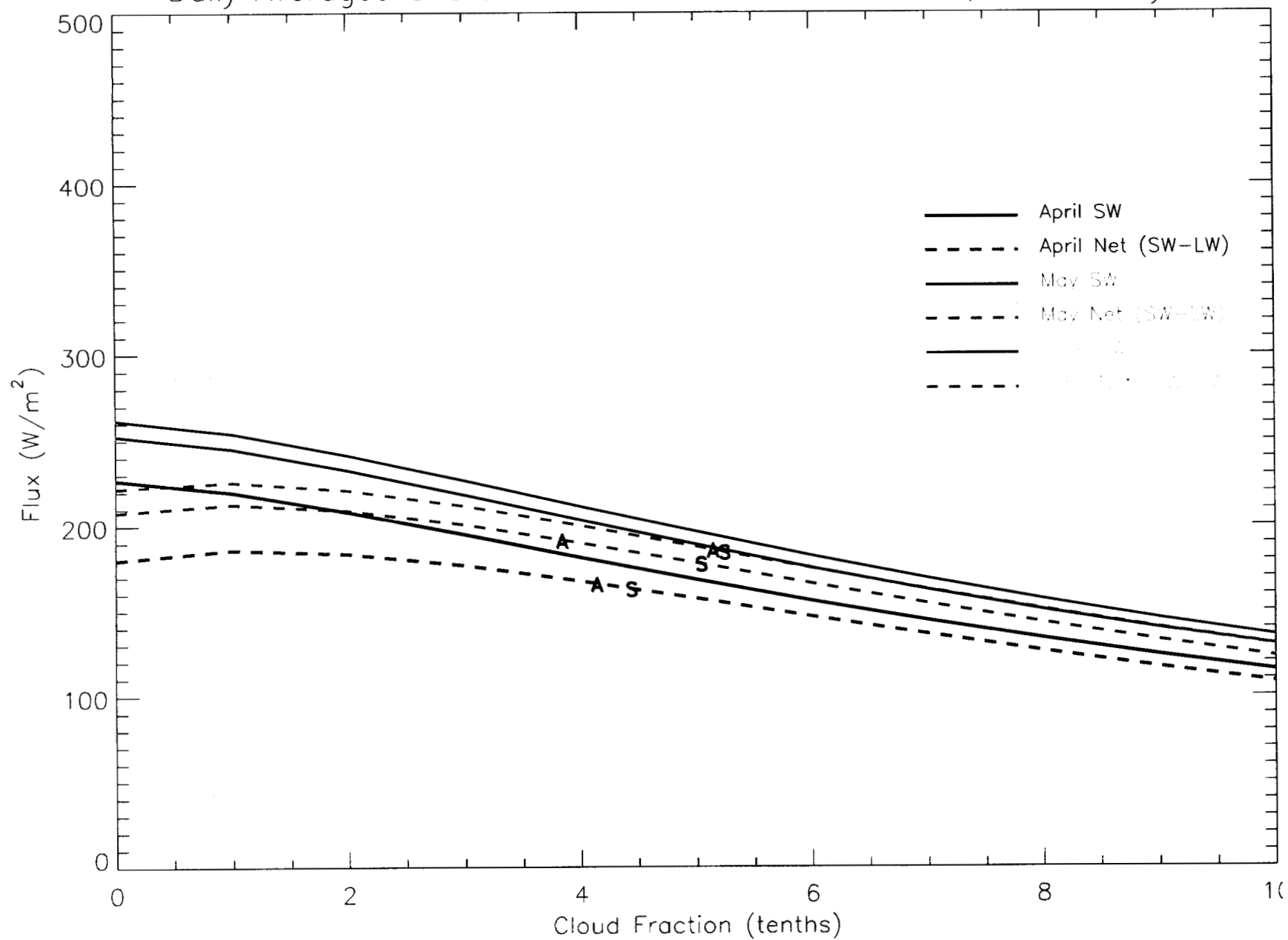


Area Averaged Latent Heat Flux and NSCAT Wind

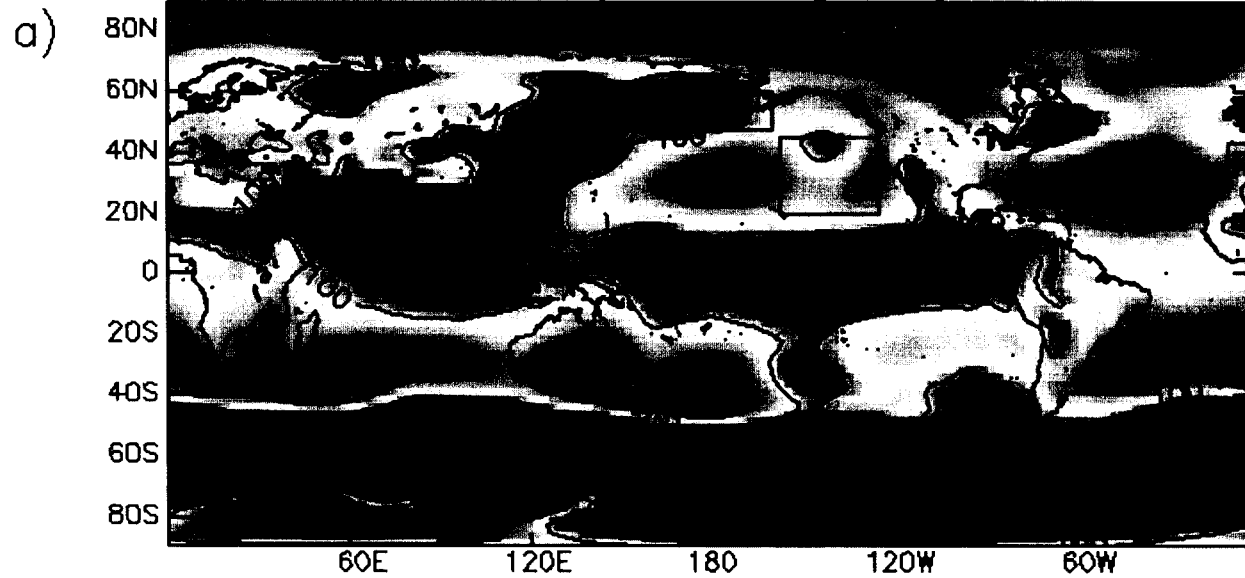




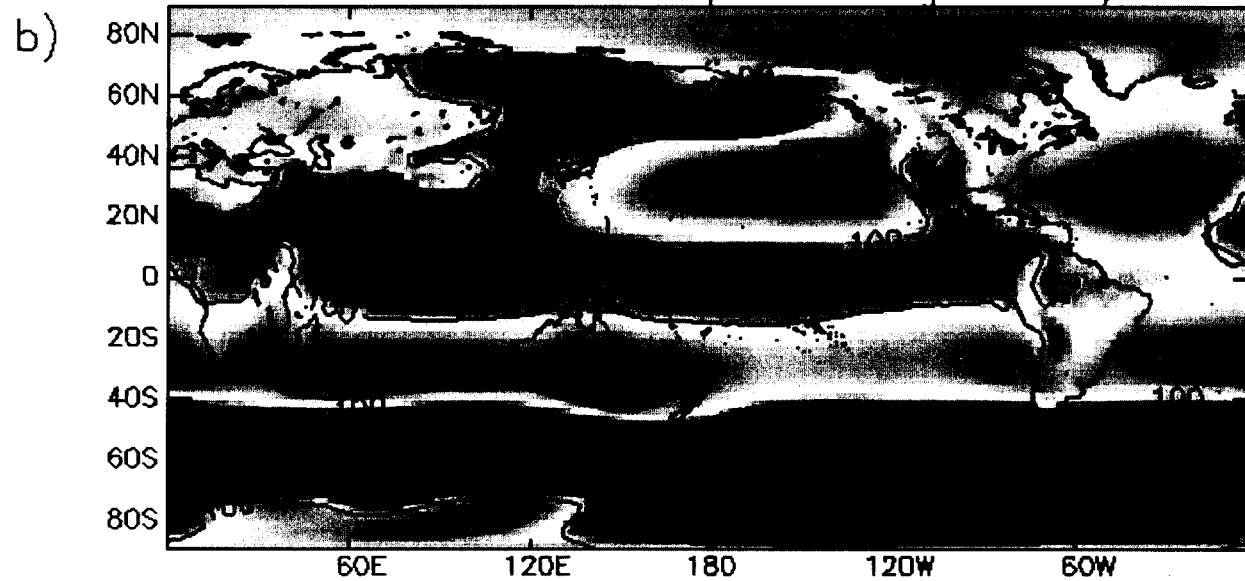
Daily Averaged Shortwave and Net Radiative Fluxes, 3 cloud layers



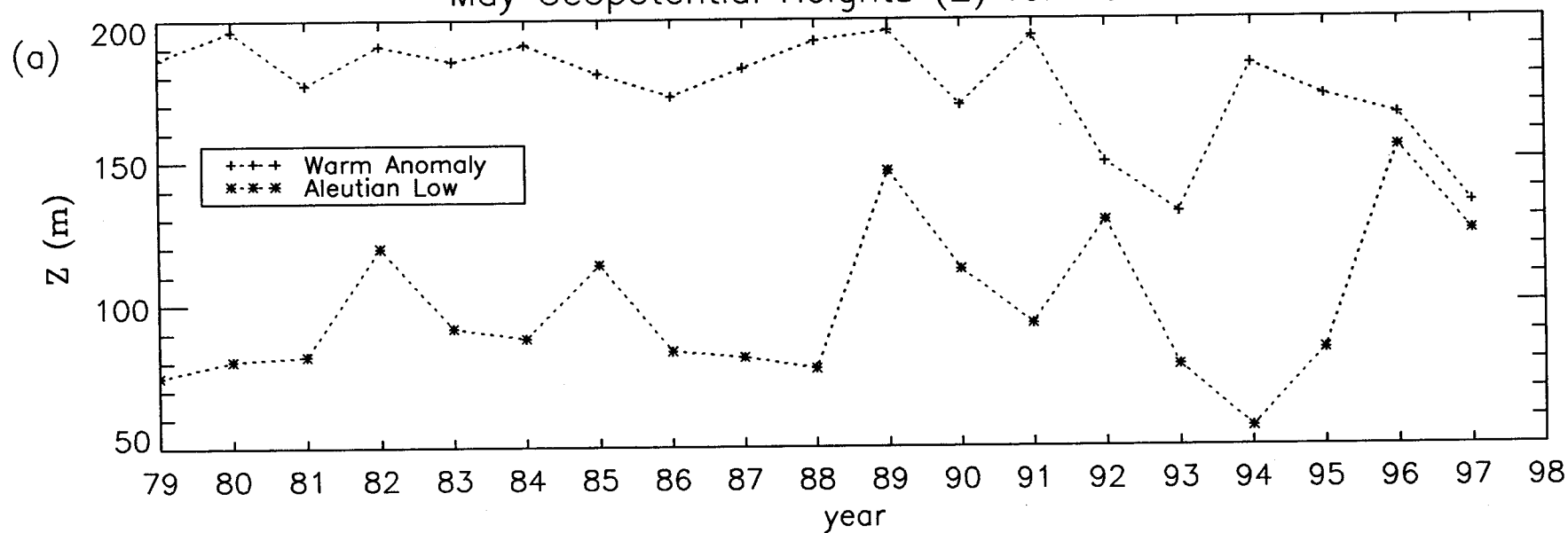
1000 mb Geopotential Height, May 1997



Seasonal 1000 mb Geopotential Height for May



May Geopotential Heights (Z) for 1979–97



May Geopotential Height Index for 1979–97

